

Exceptional points and symmetry recovery in coupled ferromagnetic waveguides

Xu-Lin Zhang,^{1,2} Shubo Wang,¹ Wen-Jie Chen,¹ and C. T. Chan^{1,*}

¹*Department of Physics and Institute for Advanced Study, The Hong Kong University of Science and Technology, Clear Water Bay, Hong Kong, China*

²*State Key Laboratory on Integrated Optoelectronics, College of Electronic Science and Engineering, Jilin University, Changchun, China*

*Corresponding author: phchan@ust.hk

We consider a two-state system consisting of a pair of coupled ferromagnetic waveguides. A monotonically increasing bias magnetic field can dynamically manipulate the system to enter a PT -symmetry broken phase and then reenter a symmetric phase. The symmetry recovery is enabled by the presence of accidental degeneracy points when the system has no loss, and each degeneracy point can spawn a pair of exceptional points when asymmetric loss is introduced. We perform microwave experiments to demonstrate the presence of the exceptional point and symmetry recovery.

Non-Hermitian systems can possess real eigenvalues if their complex potential has parity-time (PT) symmetry [1]. The system undergoes a transition at an “exceptional point” (EP) when the degree of non-Hermiticity is increased [2-4], after which the real parts of the eigenvalues coalesce while the imaginary parts bifurcate. In optics, PT symmetry can be realized if the system possesses the symmetry $\varepsilon(x) = \varepsilon^*(-x)$ and $\mu(x) = \mu^*(-x)$ [5]. EPs can also be found in passive non-Hermitian systems with asymmetric loss, which can be viewed as PT -symmetric systems with a background of uniform loss [6]. EP physics can lead to many interesting phenomena and applications such as unusual beam dynamics [7,8], lasing effects [9-12], unidirectional transmissions [13,14], asymmetric mode switching [15], and others [16-23]. EPs are typically created by tuning gain and loss. When gain and loss are increased relative to coupling strength, there is only one EP for a two-state linear system, and the PT -symmetric state cannot be recovered once the system has entered the symmetry broken phase. However, the system can reenter the PT -symmetric phase if the system has more than two states [21,24,25] or if the system is nonlinear [26,27].

In this work, we report the first experimental observation of an EP and a subsequent symmetry recovery in a two-state system by tuning an external parameter adiabatically. We first investigate a PT -symmetric coupled ferromagnetic waveguide system in the presence of a bias magnetic field. The system possesses multiple degeneracy points (DPs), which are diabolical points due to the absence of mode couplings at specific field strengths. Each DP becomes a pair of EPs of opposite chirality when gain and loss are introduced. As a result, the system carries multiple EPs and exhibits symmetry recovery behaviors in a dynamical process when the external field is tuned. When gain and loss are further increased, two EPs can merge to form a single DP again. Using a pair of waveguides, we experimentally demonstrate the presence of a pair of EPs originating from a single DP at microwave frequencies. Experimental measurements on the transmission spectra clearly show a region exhibiting enhanced transmission, which indicates the presence of the EP as well as symmetry recovery.

We start by showing the physical mechanism underlying the presence of multiple EPs for a two-state system. Figure 1(a) illustrates the PT -symmetric coupled ferromagnetic waveguide system with balanced gain and loss [$\varepsilon_1 = 12.3 - i\gamma$, $\varepsilon_2 = 12.3 + i\gamma$]. Static magnetic fields are applied to the two waveguides along opposite directions,

inducing a diagonal term μ_b and off-diagonal term $\pm i\chi$ of the permeability tensors [28, 29]. The background material is assumed to have $\epsilon_3 = 12$ and $\mu_3 = 1$. For simplicity's sake, we first set $\mu_b = 1$, which does not affect the underlying physics. We calculate the dispersions of the weakly guided modes in this paraxial waveguide system without gain and loss ($\gamma = 0$) using COMSOL [30]. Figure 1(b) shows the effective mode index, defined as $n_{eff} = \beta_z/k_0$, with β_z and k_0 denoting the mode propagation constant and vacuum wave number respectively, for the fourth pair of symmetric and anti-symmetric modes as a function of χ (solid lines). Here χ depends on the external magnetic field, as will be stipulated later. For comparison, we show the dispersion of the fourth mode in a single waveguide (dashed line), which crosses the coupled symmetric/anti-symmetric modes at two DPs. The mode degeneracy phenomenon has been reported in ferromagnetic waveguides in the presence of an external magnetic field due to the absence of mode couplings [31]. To substantiate this point, we define a mode coupling coefficient $\eta = \iint (\mathbf{E}_1 \mathbf{D}_2^* + \mathbf{H}_1 \mathbf{B}_2^*) d\sigma$ to represent the coupling strength between the two waveguides, where the subscript j corresponds to the uncoupled eigenfield in the system with only waveguide j . Figure 1(c) shows the coupling coefficient between the uncoupled fourth set of modes. We find two regions with vanishing coupling strengths that match well with the two DPs in Fig. 1(b). The absence of mode couplings in this system can be attributed to the mode symmetry transition induced by the transverse bias magnetic fields from linear polarization to elliptical polarization (see Supplemental materials for a detailed discussion on the origin of the DPs as well as the behaviors of other order modes, [29]).

The coupled waveguide system without gain and loss can be described by a Hamiltonian of the form $H = \begin{bmatrix} \beta_0 & \kappa \\ \kappa^* & \beta_0 \end{bmatrix}$, where β_0 is the propagation constant of an uncoupled mode in the single waveguide and κ denotes the couplings between the two uncoupled modes. We use the numerical results in Fig. 1(b) to fit κ as a function of χ . Figure 2(a) plots the fitted curve (solid line), showing that κ displays a similar dependence on χ as the coupling coefficient η in Fig. 1(c). We then introduce gain and loss into the system. We show three cases of gain and loss ($\gamma = 3 \times 10^{-4}$, 4.9×10^{-4} , 2×10^{-3}) in Figs. 2(b)-(d) respectively, where the effective mode index becomes complex. A PT -broken phase emerges at an EP when the gain or loss parameter becomes larger than the coupling. As the coupling is vanishing at the DPs, we expect that even a very small

γ can give rise to EPs. This is indeed the case, as shown in Fig. 2(b), where a small $\gamma = 3 \times 10^{-4}$ is sufficient to turn each DP into a pair of EPs. For ordinary two-level systems, there is only one EP and the PT -symmetry of eigenmodes remains broken beyond the EP. However, as χ increases, our system first enters a PT -broken phase but reenters a PT -symmetric phase before becoming PT -broken again. PT -symmetry recovery has been reported in multi-state systems [21,24,25], but it occurs here in a two-state system. When the gain or loss reaches a particular threshold ($\gamma = 4.9 \times 10^{-4}$), the right-handed EP of the left bubble and the left-handed EP of the right bubble merge to form a DP, as shown in Fig. 2(c). Distinct from ordinary diabolical points which have a linear crossing of the real eigenvalues, the linear crossing occurs for the imaginary parts for this DP (Fig. 2(c)). Increasing γ further, the two PT -broken phase regions merge into one so that the bubble of broken symmetry regime broadens (Fig. 2(d)). The corresponding chirality of the EPs is shown in Figs. 2(b)-(d). To better understand the variation of the eigenmode behaviors, we plot the calculated magnitude of the imaginary part of the propagation constant (defined as $\beta_r \pm i\beta_i$) in a single waveguide for the above three cases of gain and loss in Fig. 2(a) (see dashed lines). We see that the regimes corresponding to $|\kappa| < \beta_i$ match well with the numerically obtained PT -broken phase regimes in Figs. 2(b)-(d).

In fact, a system with asymmetric losses (rather than exact PT -symmetry) already exhibits the aforementioned effects. We design a non-Hermitian passive system consisting of a pair of yttrium iron garnet (YIG) waveguides working at microwave frequencies. Microwave absorbers are attached to the side of YIG waveguide 2 (red region in Fig. 3(a)) to introduce asymmetric losses into the system, given that the intrinsic dielectric loss of YIG is negligible. We apply a bias magnetic field along the negative x -axis. The eigenfield distributions move towards the $+y$ interface due to the field displacement effect when the transverse bias magnetic field is perpendicular to the RF magnetic field [28]. EPs and symmetry recovery can also appear in this configuration due to the field-induced variation of mode couplings. We first theoretically analyze the eigenmodes supported in this system. The permeability tensor of YIG is modeled with $\mu_b = 1 + \omega_m \omega_0 / (\omega_0^2 - \omega^2)$ and $\chi = \omega_m \omega / (\omega_0^2 - \omega^2)$, where $\omega_0 = \mu_0 \gamma_R H_0$ is determined by the gyromagnetic ratio γ_R and bias magnetic field H_0 , and $\omega_m = \mu_0 \gamma_R M$ is determined by the magnetization M , which is measured experimentally [29]. Here, permeability losses can be ignored because the system works far away from

the gyromagnetic resonance. Figure 3(b) shows the calculated effective mode index of the coupled YIG waveguides at 9.5 GHz as a function of the bias magnetic field. In the simulation, the permittivity of YIG and the microwave absorber are chosen as ~ 15.2 [32] and $\sim 4+15i$ [29] respectively. We find a region (0.02 T \sim 0.16 T) where the real parts of the two modes almost coalesce while the corresponding imaginary parts first repel and then approach each other again. This is a typical feature of an EP associated with symmetry recovery, although here the real/imaginary parts are separated in the broken/symmetric phase region due to the mode detuning induced by the broken symmetry of the two waveguides (only one waveguide is attached with the microwave absorber). In other words, the system is very close to the exact EP and symmetry recovery point [29]. The inset of Fig. 3(b) shows the presence of a DP when the microwave absorber is removed. This DP spawns a pair of EPs of opposite chirality when asymmetric losses are introduced and symmetry recovery naturally arises. The power flow distributions of the eigenmodes are also illustrated in the inset of Fig. 3(b), where the field displacement effect can be found. The symmetry of the eigenmode (*PT*-symmetric/broken) is also evident.

We then perform microwave experiments to implement the theoretical design. A photograph of the experimental setup is shown in Fig. 4(a), where a pair of YIG waveguides (8 mm \times 4 mm \times 200 mm) with a gap of ~ 0.5 mm are placed inside a vibrating sample magnetometer, which can provide a quasi-uniform bias magnetic field along the negative x -axis in the area of interest. The transmission spectra of the system are measured to identify the EP as well as the symmetry recovery behavior, since the transmission is enhanced in the broken phase region [6]. An antenna is placed near the surface of the lossy waveguide to excite both the symmetric and anti-symmetric modes in the system, while another is used on the other side to receive the transmission power. The measured transmission spectra for different magnetic field strengths are plotted in Fig. 4(b). The results for the lossless system are given for reference (see the dotted line), confirming the absorber's effectiveness. We mainly focus on the frequency range above 6.5 GHz, below which the anti-symmetric mode is cut off. In the frequency range of interest, we observe considerable transmission enhancement when the bias magnetic field is increased. The enhanced transmission regime corresponds to the symmetry broken phase, in which the wave can travel a longer distance in the waveguide without the absorber. We note that enhanced transmission is observed for higher frequencies in

lower fields (~ 0.1 T) and for lower frequencies in higher fields (~ 0.2 T). The transmission finally drops to low values at ~ 0.3 T.

To further investigate the transmission behavior, we plot the transmission power as a function of the bias magnetic field at 9.5 GHz in Fig. 4(e) (see circles). We find a region (0.04 T \sim 0.18 T) exhibiting enhanced transmission that matches well with the broken phase region predicted in Fig. 3(b). We also perform a numerical simulation for the system at 9.5 GHz. A line current source (white lines in Fig. 3(d)) is placed near the edge of the lossy waveguide to mimic the antenna in experiments. The power flow S_z at the output surface is then integrated to provide the transmission. The calculated transmission spectrum of the system with a length of 200 mm, which can reproduce the salient features observed in experiments, is shown in Fig. 3(c). The transmission exhibits an oscillating behavior in both experiments and simulations due to the Fabry-Perot resonance associated with the change in effective mode index under the variation of the bias magnetic field for a waveguide of a finite length. A further increase in the waveguide length to 400 mm in the simulation can double the resonant peak number (see Fig. 3(c)), confirming the presence of the Fabry-Perot effect. To show the origin of the transmission enhancement in the broken phase region, we illustrate in Fig. 3(d) the calculated power flow distributions for four cases marked (i)-(iv) in Fig. 3(c). For cases (i) and (iv), the system operates in the symmetric phase regime and the power flow decays exponentially along the direction of propagation. On the contrary, the system in case (ii) is in the broken phase region, and the two eigenmodes propagate individually in the two waveguides. The transmission of the whole system is then increased as a result of the longer transport distance in the lossless waveguide 1. While the transmission in case (iii) dips due to destructive Fabry-Perot interference, there remains a stable power flow in waveguide 1, indicating that the system is still operating in the broken phase region. We also note that after the broken phase region, the transmission again increases when the field is greater than 0.2 T (see Fig. 4(e) for experiment and 3(c) for simulation). This is due to the overall decrease in mode losses (see the imaginary part in Fig. 3(b)) as field strength increases because a stronger external field can displace the eigenfield from the absorber (see the field patterns in Fig. 3(b)). A further increase in the external field drives the two eigenmodes close to the cutoff (see the real part in Fig. 3(b); also refer to Fig. 4(c)) as μ_b approaches zero [28]. As a result, the transmission shows a sudden drop.

We provide more experimental evidence on the EPs by studying the case of 7.5 GHz (circles in Fig. 4(f)), where the broken phase region can also be identified by an enhanced transmission. Unlike the case of 9.5 GHz, a higher bias magnetic field is required at 7.5 GHz in order to reach the broken phase region. From the experimental results of transmission versus bias magnetic field at various frequencies, we can locate the external field required to reach the center of the enhanced transmission region for each frequency, corresponding to the center of the broken phase region. The required field strength is then plotted in the form of circles in Fig. 4(c), and they show a similar dependence on frequency as the calculated external fields to reach the DP of the lossless system (solid line in Fig. 4(c)). We also calculate the bias magnetic field required for the modes to reach the cutoff (black dotted line in Fig. 4(c)), which matches well with experimental results (squares in Fig. 4(c)) with small discrepancies that can be attributed to the non-uniformity of the bias magnetic field (see Supplemental materials for a discussion on the non-uniformity effect, [29]). For 7.5 GHz, the cutoff is very close to the broken phase center, and consequently, the symmetry recovery behavior could not be observed in the experiment (circles in Fig. 4(f)), since the mode was cut off before the symmetry recovery regime could be accessed.

Finally, we provide control experiment results to further verify the presence of EPs. In the first control experiment, the coupled waveguide system is rotated by 90° around the z -axis. Since no EPs are supported in such a configuration (see Supplemental materials [29]), the aforementioned transmission enhancement phenomenon could not be observed (see Fig. 4(d) and the triangles in Figs. 4(e) and 4(f)). The second control experiment is performed by increasing the gap to 2 mm. Simulations show that EPs appear in a lower bias field with a broader broken phase region due to the shift of the DPs in the lossless system [29]. This is confirmed by the experimental results (see squares in Figs. 4(e) and 4(f)), which show that the system with a zero bias field at 9.5 GHz is already in the broken phase region. Other control experiment results are given in the Supplemental material [29]. All of the above experimental results are consistent with our theoretical predictions, demonstrating the presence of EPs as well as symmetry recovery behaviors.

To conclude, we have shown both theoretically and experimentally that in a two-state coupled ferromagnetic waveguide system, EPs can be manipulated by tuning a bias magnetic field, creating multiple EPs and symmetry recovery behaviors that are

rarely seen in two-state systems. Compared to conventional EP systems based on tuning gain and loss, the tuning process in this work is both adiabatic and continuous. This process can be employed to tune system parameters to encircle an EP to manifest the topological properties of the system [15,33,34] and may be applicable to the non-reciprocal transport of electromagnetic waves and communications.

ACKNOWLEDGEMENTS

This work is supported by the Hong Kong Research Grants Council through grant AoE/P-02/12. Xu-Lin Zhang is also supported by the National Natural Science Foundation of China (Grant No. 61605056) and the China Postdoctoral Science Foundation (Grant No. 2016M591480).

REFERENCES

- [1] C. M. Bender and S. Boettcher, Phys. Rev. Lett. **80**, 5243 (1998).
- [2] I. Rotter, J. Phys. A **42**, 153001 (2009).
- [3] N. Moiseyev, *Non-Hermitian Quantum Mechanics* (Cambridge University Press, Cambridge, 2011).
- [4] W. D. Heiss, J. Phys. A **45**, 444016 (2012).
- [5] C. E. Rüter, K. G. Makris, R. El-Ganainy, D. N. Christodoulides, M. Segev, and D. Kip, Nat. Phys. **6**, 192 (2010).
- [6] A. Guo, G. J. Salamo, D. Duchesne, R. Morandotti, M. Volatier-Ravat, V. Aimez, G. A. Siviloglou, and D. N. Christodoulides, Phys. Rev. Lett. **103**, 093902 (2009).
- [7] A. Regensburger, C. Bersch, M. Miri, G. Onishchukov, D. N. Christodoulides, and U. Peschel, Nature **488**, 167 (2012).
- [8] K. G. Makris, R. El-Ganainy, D. N. Christodoulides, and Z. H. Musslimani, Phys. Rev. Lett. **100**, 103904 (2008).
- [9] B. Peng, S. K. Özdemir, S. Rotter, H. Yilmaz, M. Liertzer, F. Monifi, C. M. Bender, F. Nori, and L. Yang, Science **346**, 328 (2014).
- [10] L. Feng, Z. J. Wong, R. M. Ma, Y. Wang, and X. Zhang, Science **346**, 972 (2014).
- [11] H. Hodaei, M. Miri, M. Heinrich, D. N. Christodoulides, and M. Khajavikhan, Science **346**, 975 (2014).
- [12] M. Brandstetter, M. Liertzer, C. Deutsch, P. Klang, J. Schöberl, H. E. Türeci, G. Strasser, K. Unterrainer, and S. Rotter, Nat. Commun. **5**, 4034 (2014).
- [13] Y. D. Chong, L. Ge, and A. D. Stone, Phys. Rev. Lett. **106**, 093902 (2011).
- [14] L. Ge, Y. D. Chong, S. Rotter, H. E. Türeci, and A. D. Stone, Phys. Rev. A **84**, 023820 (2011).
- [15] J. Doppler, A. A. Mailybaev, J. Böhm, U. Kuhl, A. Girschik, F. Libisch, T. J. Milburn, P. Rabl, N. Moiseyev, and S. Rotter, Nature **537**, 76 (2016).
- [16] S. Longhi, Phys. Rev. Lett. **103**, 123601 (2009).
- [17] R. Fleury, D. L. Sounas, and A. Alù, Phys. Rev. Lett. **113**, 023903 (2014).
- [18] J. Wiersig, Phys. Rev. Lett. **112**, 203901 (2014).
- [19] Y. Sun, W. Tan, H. Q. Li, J. Li, and H. Chen, Phys. Rev. Lett. **112**, 143903 (2014).
- [20] L. Chang, X. Jiang, S. Hua, C. Yang, J. Wen, L. Jiang, G. Li, G. Wang, and M. Xiao, Nat. Photon. **8**, 524 (2014).
- [21] K. Ding, G. Ma, M. Xiao, Z. Q. Zhang, and C. T. Chan, Phys. Rev. X **6**, 021007 (2016).
- [22] B. Dietz, H. L. Harney, O. N. Kirillov, M. Miski-Oglu, A. Richter, and F. Schäfer, Phys. Rev. Lett. **106**, 150403 (2011).
- [23] B. Zhen, C. W. Hsu, Y. Igarashi, L. Lu, I. Kaminer, A. Pick, S. L. Chua, J. D. Joannopoulos, and M. Soljačić, Nature **525**, 354 (2015).
- [24] N. X. A. Rivolta and B. Maes, Opt. Lett. **40**, 3922 (2015).
- [25] H. Benisty, A. Lupu, and A. Degiron, Phys. Rev. A **91**, 053825 (2015).
- [26] Y. Lumer, Y. Plotnik, M. C. Rechtsman, and M. Segev, Phys. Rev. Lett. **111**, 263901 (2013).
- [27] A. U. Hassan, H. Hodaei, M. A. Miri, M. Khajavikhan, and D. N. Christodoulides, Phys. Rev. A **92**, 063807 (2015).
- [28] D. M. Pozar, *Microwave Engineering* (Wiley, New York, 2005).
- [29] See Supplemental Material for (i) detailed study on the origin of the degeneracy points, (ii) exact exceptional point and symmetry recovery point in the YIG system, (iii) material property of YIG and the microwave absorber, (iv) some control experimental results, (v) non-uniformity effect of the bias magnetic field.
- [30] www.comsol.com.

- [31] A. B. Yakovlev and G. W. Hanson, IEEE Trans. Microwave Theory Tech. **51**, 583 (2003).
- [32] Y. Poo, R. X. Wu, Z. Lin, Y. Yang, and C. T. Chan, Phys. Rev. Lett. **106**, 093903 (2011).
- [33] H. Xu, D. Mason, L. Jiang, and J. G. E. Harris, Nature **537**, 80 (2016).
- [34] T. J. Milburn, J. Doppler, C. A. Holmes, S. Portolan, S. Rotter, and P. Rabl, Phys. Rev. A **92**, 052124 (2015).

Figures and captions

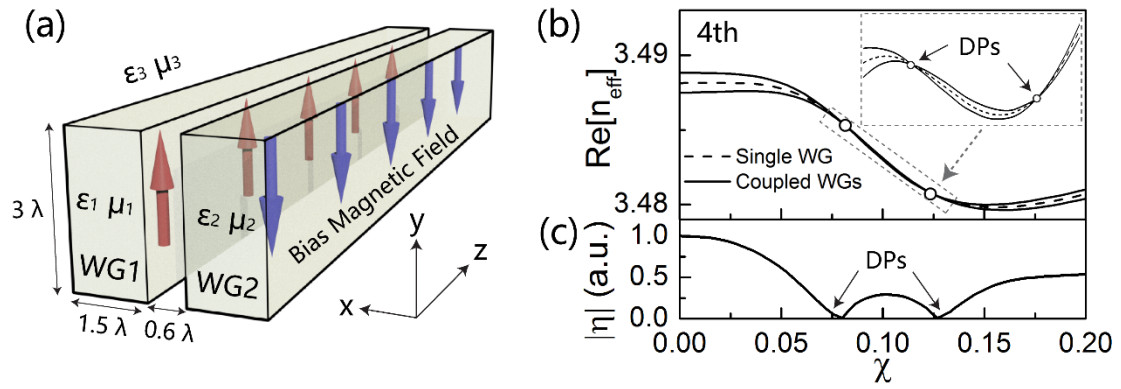


Figure 1 (a) Schematic of the coupled ferromagnetic waveguide system with bias magnetic fields applied along opposite directions. (b) Calculated effective mode index of the fourth pair of modes in the coupled system (solid lines) and that of the fourth mode in a single waveguide (dashed line) as a function of χ with $\gamma = 0$, where we find two degeneracy points. (c) Calculated mode coupling coefficient $|\eta|$ (see text for definition).

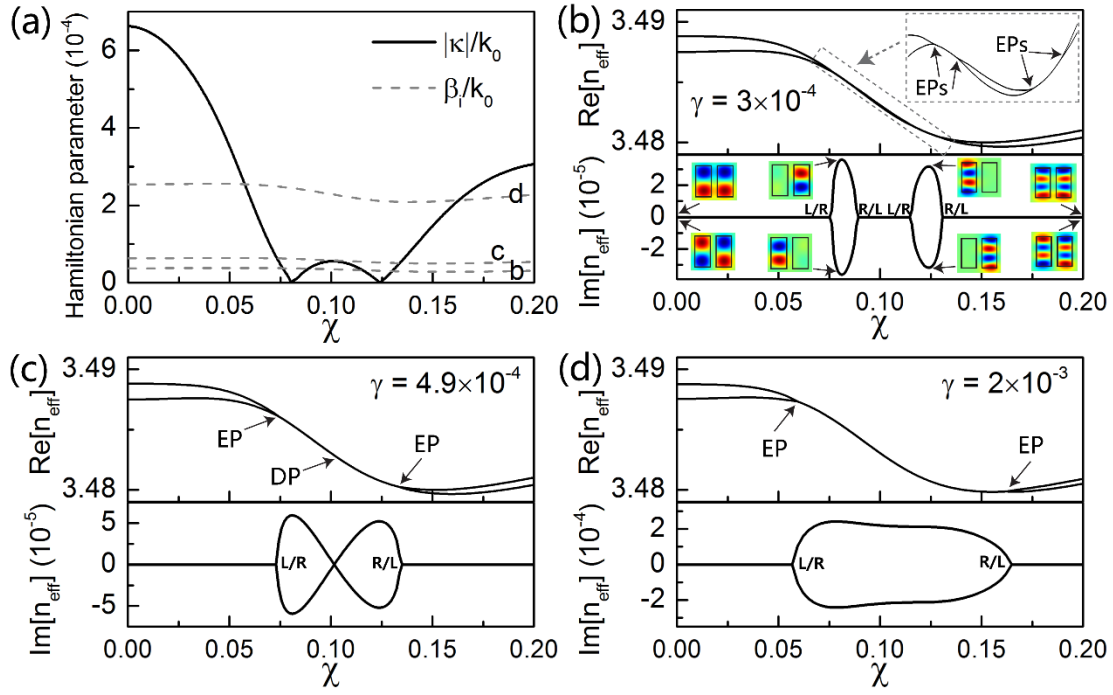


Figure 2 (a) The coupling parameter κ (solid line) obtained through fitting for the fourth pair of modes in the system without gain and loss. The dashed lines show the calculated imaginary part of the effective mode index of the fourth mode in a single waveguide with gain and loss corresponding to those in (b)-(d). (b)-(d) Calculated effective mode index of the fourth pair of modes with different gain and loss, (b) $\gamma = 3 \times 10^{-4}$, (c) $\gamma = 4.9 \times 10^{-4}$, and (d) $\gamma = 2 \times 10^{-3}$. We find multiple EPs and symmetry recovery behaviors. The inset of (b) shows H_y eigenfield distributions at different χ , showing features typical of PT -symmetric and PT -broken regions.

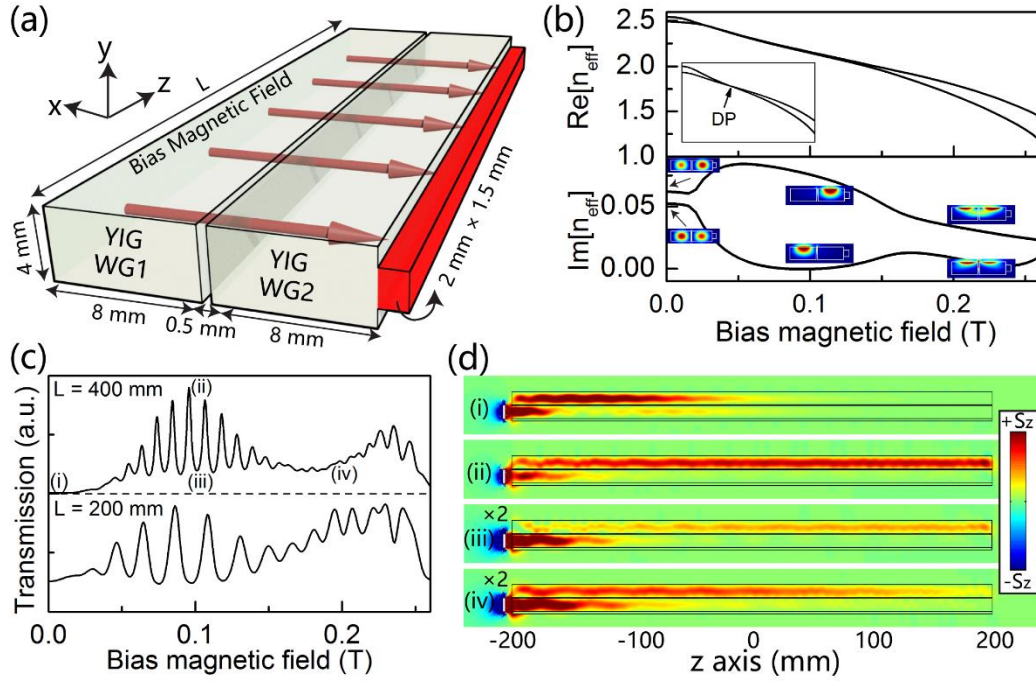


Figure 3 (a) Schematic of a passive coupled YIG waveguide system with microwave absorbers attached to the side of one waveguide. (b) Calculated effective mode index as a function of the bias magnetic field, in which we find the salient feature of an EP as well as symmetry recovery. The upper inset shows the results for the lossless coupled system, where a DP appears and can spawn a pair of EPs when an absorber is added. The lower inset shows the power flow distributions in different bias magnetic fields. (c) Numerically simulated transmission spectra as a function of the magnetic field for $L = 200$ mm and 400 mm, where a region with enhanced transmission can be found that matches well with the broken phase region predicted in (b). The peaks correspond to Fabry-Perot resonances. (d) Power flow distributions in the coupled system with $L = 400$ mm for different magnetic fields marked as (i)-(iv) in (c). The field patterns in (iii) and (iv) have been scaled up by a factor of two for improved readability. The frequency is 9.5 GHz in all of these simulations.

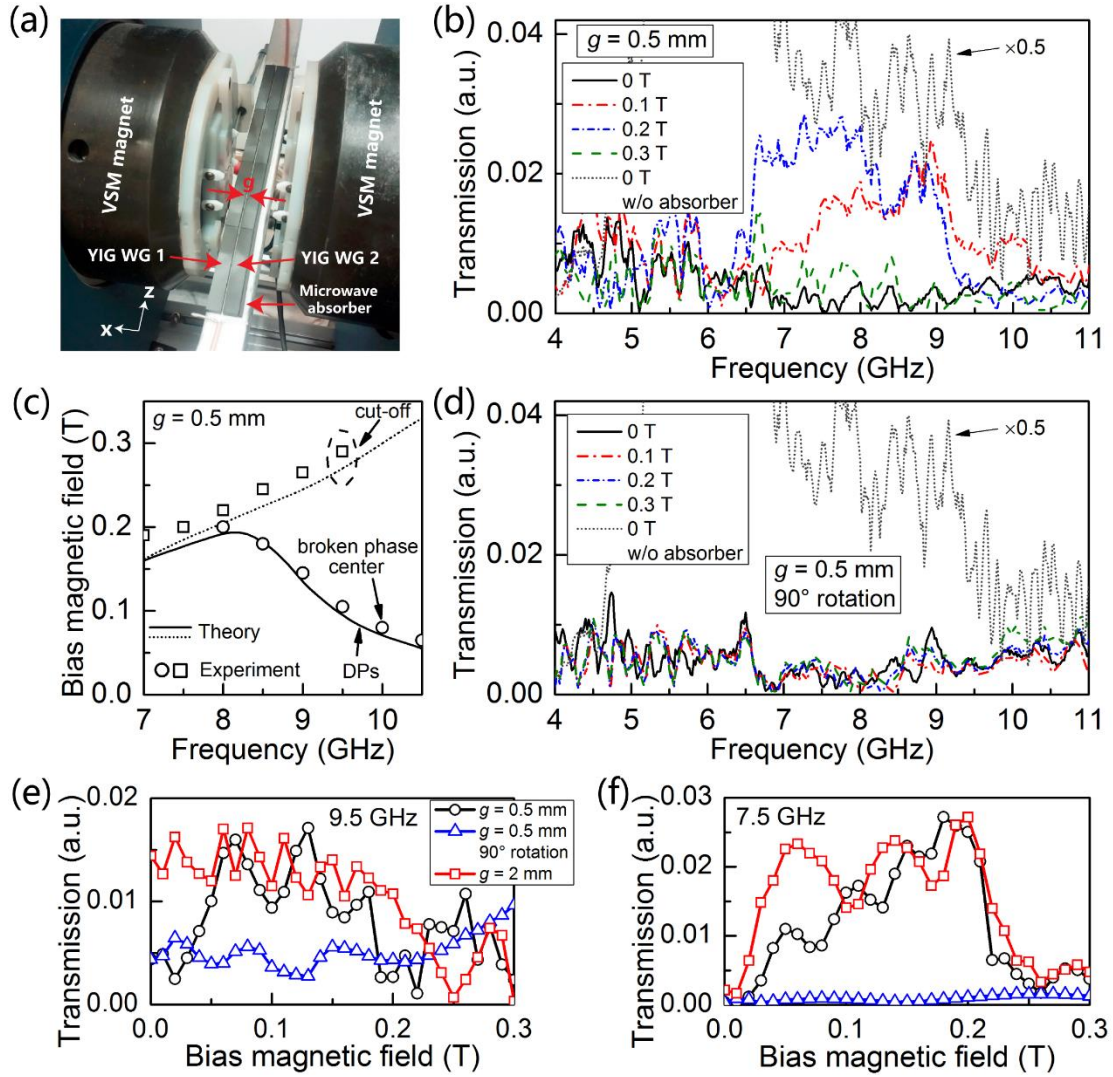


Figure 4 (a) A photograph of the coupled YIG waveguide system placed inside a vibrating sample magnetometer. Microwave absorbers are attached on the side of one waveguide. Each waveguide measures $8 \text{ mm} \times 4 \text{ mm} \times 200 \text{ mm}$ and the gap is $g = 0.5$ mm. (b) Measured transmission spectra for different magnetic field strengths. The spectrum for the lossless system is also given for reference. (c) Experimentally estimated center of the transmission enhancement region of the lossy system (circles), showing a similar dependence on frequency as the calculated external field required to reach the DP in the lossless system (solid line). The dotted line and squares show the calculated and experimentally estimated bias magnetic fields above which the modes would be cut off respectively. (d) Measured transmission spectra of the system in (a) but rotated by 90° around the z -axis, where no EP-related phenomena can be found. (e)-(f) Measured transmission power as a function of the bias magnetic field for (e) 9.5 GHz and (f) 7.5 GHz. The circles, squares, and triangles show the results for the system

with $g = 0.5$ mm, $g = 2$ mm, and $g = 0.5$ mm but with a 90° rotation of the waveguides around the z -axis, respectively.

Supplemental Material for “Exceptional points and symmetry recovery in coupled ferromagnetic waveguides”

Xu-Lin Zhang,^{1,2} Shubo Wang,¹ Wen-Jie Chen,¹ and C. T. Chan^{1,*}

¹*Department of Physics and Institute for Advanced Study, The Hong Kong University of Science and Technology, Clear Water Bay, Hong Kong, China*

²*State Key Laboratory on Integrated Optoelectronics, College of Electronic Science and Engineering, Jilin University, Changchun, China*

*Corresponding author: phchan@ust.hk

1 Mode analysis

In this part, we give a detailed study on the origin of the degeneracy points (DPs) in the main text. We first consider the coupled ferromagnetic waveguide system shown in Fig. 1(a). Under the bias magnetic fields, the permeability tensors take the form:

$$\mu_1 = \begin{bmatrix} \mu_b & 0 & i\chi \\ 0 & 1 & 0 \\ -i\chi & 0 & \mu_b \end{bmatrix}, \mu_2 = \begin{bmatrix} \mu_b & 0 & -i\chi \\ 0 & 1 & 0 \\ i\chi & 0 & \mu_b \end{bmatrix}. \quad (1)$$

Figure S1(a) shows the calculated effective mode index of the first four pairs of modes as a function of χ . Each pair of modes consist of a symmetric and an anti-symmetric mode as a result of waveguide couplings. We find multiple DPs can be supported in the system (see the circles) due to the absence of mode couplings at specific values of χ . To further explore the origin of the absence of mode couplings, we study a single ferromagnetic waveguide under a bias magnetic field (see the inset of Fig. S1(b)) and show the corresponding effective mode index as a function of χ in Fig. S1(b). The variation of the eigenfield characteristics of the single waveguide mode under a bias magnetic field should account for the origin of DPs. To show this point, we illustrate in Fig. S1(c) the magnetic field distributions H_x and H_y in the single waveguide for the first four modes with $\chi = 0$ (upper figures) and $\chi = 0.2$ (lower figures). The eigenfields along the propagating z -axis in this paraxial waveguide ($\varepsilon_1 \approx \varepsilon_3$) are nearly zero so that they are not shown here. When the bias field is absent ($\chi = 0$), the eigenmodes are linearly polarized, and the 1st, 2nd, 3rd and 4th mode are E_y/H_x , E_x/H_y , E_y/H_x and E_x/H_y polarized, respectively. The polarization of the eigenmodes becomes elliptical (as evidenced by the co-existence of x - and y -field components) when applied with a transverse bias field as shown by the results with χ

$= 0.2$. Then we see a significant change of the eigenmode characteristics, i.e., from linear polarization to elliptical polarization upon increasing the bias magnetic field. Since the bias magnetic field in the two waveguides is along opposite direction, in the above transition process the corresponding eigenfields should change in a different way which results in the absence of mode couplings associated with DPs. The absence of mode couplings at a specific value of $\chi = 0.0816$ can be understood from Fig. S2, where we show the field distributions of the two uncoupled fourth set of modes, corresponding to the first DP of the fourth pair of modes in Fig. S1(a). An integration of the two uncoupled eigenfields via $\eta = \iint (\mathbf{E}_1 \mathbf{D}_2^* + \mathbf{H}_1 \mathbf{B}_2^*) d\sigma$ gives a zero coupling strength. The z -component of the eigenfield is very small and therefore not shown here.

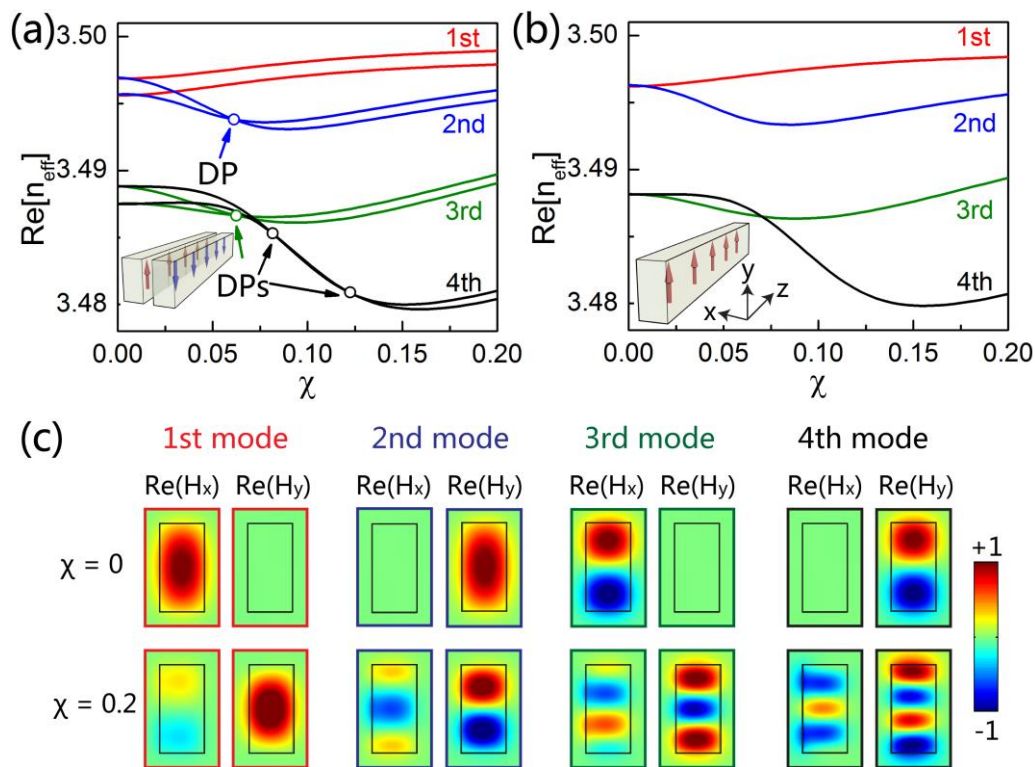


Figure S1. (a) Calculated effective mode index of the first four pairs of modes in the coupled waveguides as a function of χ . (b) Calculated effective mode index of the first four modes in the single waveguide as a function of χ . (c) Magnetic field distributions for the first four modes in the single waveguide with $\chi = 0$ and 0.2.

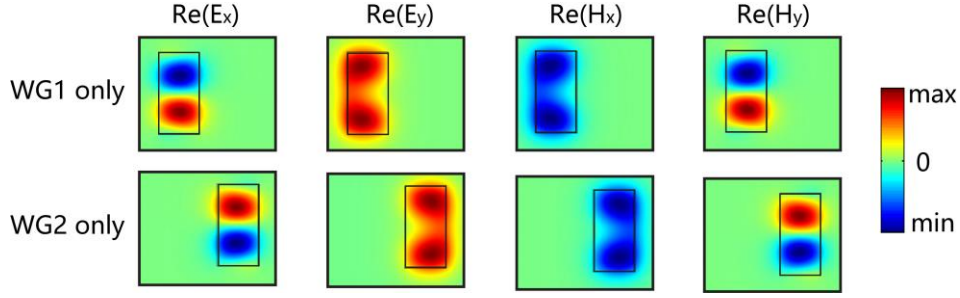


Figure S2. Eigenfield patterns of the two uncoupled fourth set of modes in a single waveguide with $\chi = 0.0816$. At the same value a DP appears between the fourth pair of modes in the coupled waveguides. The integration of the field patterns gives a zero coupling strength. So, if we use the eigenmodes of a single waveguide to predict the DP of coupled waveguides, in the spirit of standard perturbation theory, we will predict a value of $\chi = 0.0816$.

We can follow the same way to demonstrate the presence of a DP in the coupled YIG waveguide system shown in Fig. 3(a). We calculate the coupling strength and show the result in Fig. S3(a). The vanishing coupling strength at ~ 0.095 T can account for the DP in the inset of Fig. 3(b). We further show in Fig. S3(b) the eigenfield patterns of the two uncoupled modes in a single YIG waveguide at this DP. The integration between the two eigenfields via $\eta = \iint (\mathbf{E}_1 \mathbf{D}_2^* + \mathbf{H}_1 \mathbf{B}_2^*) d\sigma$ is exactly zero at this point.

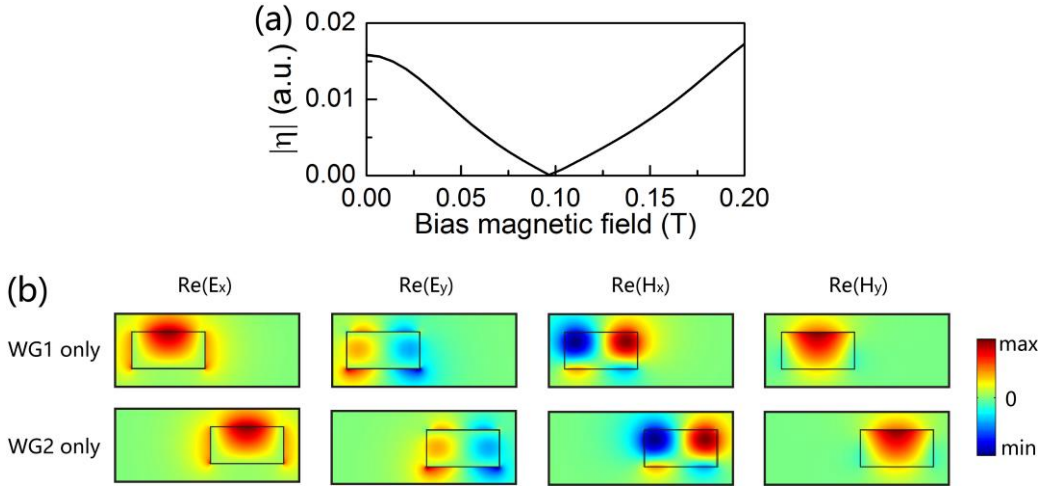


Figure S3. (a) Coupling coefficient between the two uncoupled fundamental modes in the coupled system shown in Fig. 3(a). The frequency is 9.5 GHz. (b) Eigenfield patterns of the two uncoupled modes in a single YIG waveguide with a bias magnetic field of ~ 0.095 T, corresponding to the case of the DP in (a).

2 Exact EP and symmetry recovery point in the YIG system

In Fig. 3(b) the exact exceptional point (EP) and symmetry recovery point are actually not found because of the broken symmetry of the system, i.e., only one waveguide is attached with the microwave absorber. We can only say that our system is very close to the exact EPs. In this part, we show theoretically that the exact EPs can be reached if we slightly tune the width of YIG waveguide 2. The studied system is shown in Fig. S4(a) where W denotes the width of YIG waveguide 2. We then tune W and find the exact EP and symmetry recovery point can be accessed with $W = 8.014$ mm and $W = 7.704$ mm, as shown in Fig. S4(b) and S4(c), respectively. Although the exact EPs can hardly be accessed in experiments, creating a system that is very close to the exact EPs as we show in this work is sufficient to study the physics and consequences of EPs.

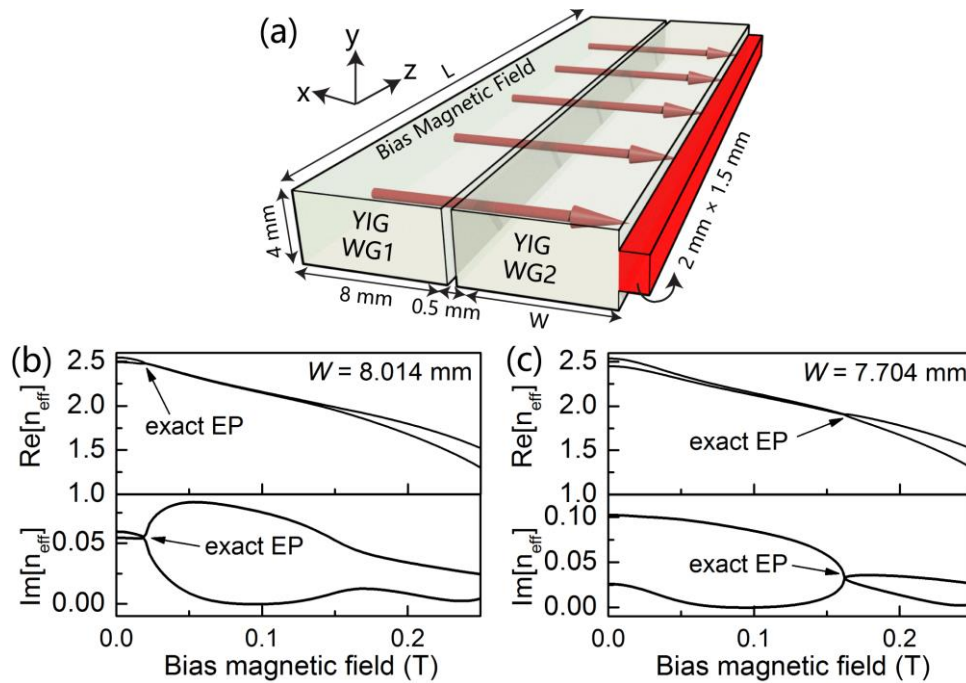


Figure S4. (a) Schematic of a YIG coupled waveguide system in which we tune the width of waveguide 2 in order to reach the exact EPs. (b) Calculated effective mode index as a function of the bias magnetic field with $W = 8.014$ mm where the exact EP can be found at 0.019 T. (c) Calculated effective mode index as a function of the bias magnetic field with $W = 7.704$ mm where the exact symmetry recovery point can be found at 0.162 T.

3 Material properties

In this part, we show the material properties of YIG and the microwave absorber. Figure S5(a) shows the measured hysteresis loop of YIG using a vibrating sample

magnetometer, where M is the measured magnetization. This curve is then used for calculating the permeability tensor of YIG. Figure S5(b) shows the permittivity of the microwave absorber which is measured using Agilent 85071C material measurement software controlled by Agilent Technologies 8720ES Network Analyzer. The permittivity is used for all the simulations in this work.

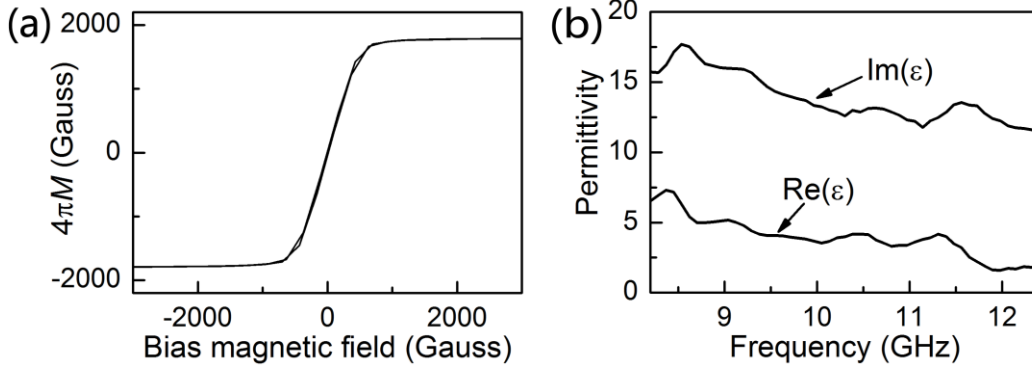


Figure S5. (a) Measured hysteresis loop of YIG. (b) Measured permittivity of the microwave absorber.

4 Control experiment I: rotating the system by 90°

We perform a control experiment in which the coupled waveguide system is rotated by 90° around the z -axis, meaning that the bias field is actually parallel to the short-edge of the YIG waveguide (see Fig. S6(a)). We calculate the effective mode index as a function of the bias magnetic field at 9.5 GHz and show the results in Fig. S6(b). We see that in the field range of interest there is no EP-related physics. This is due to the fact that the system does not possess a DP when the microwave absorber is absent (see the inset of Fig. S6(b)). The measured transmission spectra with different bias magnetic fields have already been shown in Fig. 4(d). These spectra look almost the same, indicating that no EPs or symmetry-recovery physics exist in such a configuration. This control experiment can further support our conclusion that the enhanced transmission in Fig. 4(b) is due to the presence of EPs and symmetry-recovery.

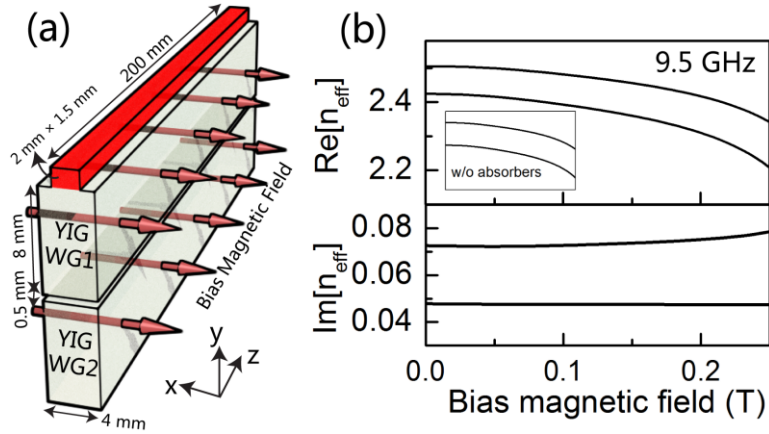


Figure S6. (a) Schematic of a coupled ferromagnetic waveguide system with the bias magnetic field parallel to the short-edge of the waveguide. (b) Calculated effective mode index as a function of the bias magnetic field. The inset shows the real part of the effective mode index in the lossless system, showing the absence of DPs.

5 Control experiment II: increasing the gap distance to 2 mm

We perform another control experiment in which the gap distance between the two YIG waveguides is increased to $g = 2$ mm. We first calculate the effective mode index of the lossless system at 9.5 GHz and show the results in Fig. S7(a). We note that the position of the DP exhibits a shift compared to the case of $g = 0.5$ mm. In other words, the DP will appear at a lower bias magnetic field when the gap distance is increased. This trend is also shown in Fig. S7(d) for different frequencies (comparing the red line and black line). The shift of the DP results in a shift of the broken phase region in the lossy system. To show this point, we plot in Fig. S7(b) the calculated imaginary part of the effective mode index. It is then not surprising to find that with a larger gap distance of 2 mm, the system with a zero bias field at 9.5 GHz is already in the broken phase region (also see the squares in Fig. 4(e)). The mode coupling becomes weaker when the gap distance is increased. As a consequence, with the same microwave absorber attached, the bandwidth of the broken phase region becomes broader (see Fig. S7(b) for theoretical results, Figs. 4(e) and 4(f) for experimental phenomena and Fig. 2(a) for interpretation). Figure S7(c) shows the measured transmission spectra of the 2 mm-gap system with different bias magnetic fields, confirming the above theoretical analysis. All of the results shown in this part can help better understand the experimental results in Figs. 4(e) and 4(f).

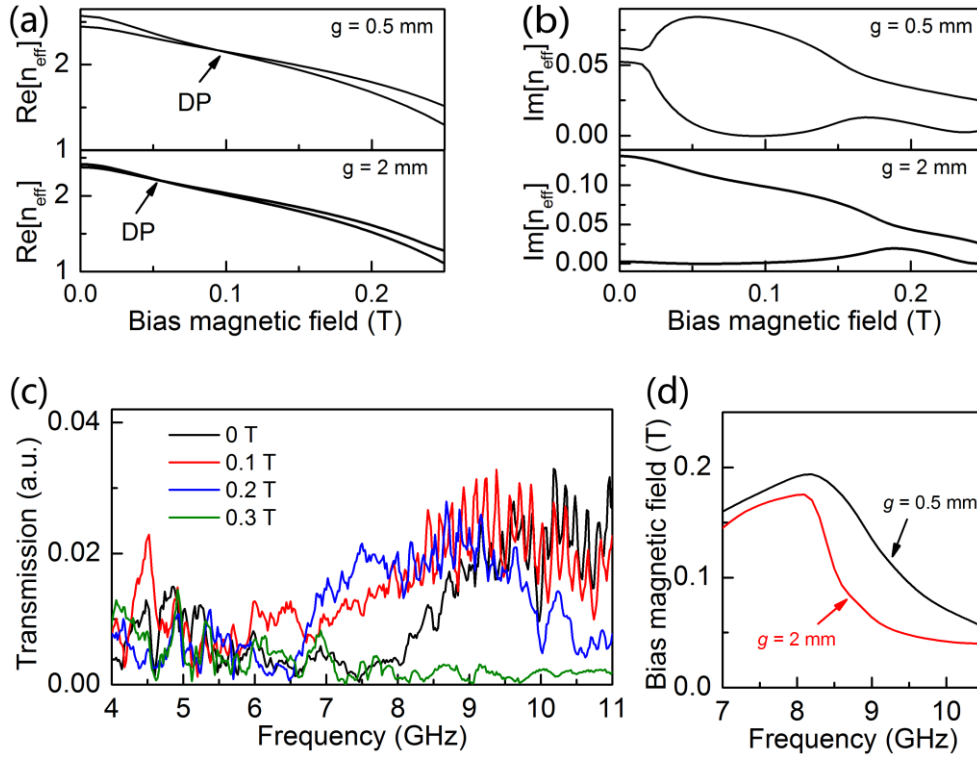


Figure S7. Calculated effective mode index as a function of the bias magnetic field in the lossless system (a) and lossy system (b) with different gap distances at 9.5 GHz. (c) Measured transmission spectra of the 2 mm-gap system with different bias magnetic fields. (d) Calculated bias magnetic field required to reach the DP in the lossless system with $g = 0.5$ mm and $g = 2$ mm.

6 Control experiment III: removing the microwave absorber

We perform a third control experiment in which the microwave absorber is removed, as illustrated schematically in Fig. S8(a). The aim of this control experiment is to demonstrate that the observed transmission enhancement phenomenon is not simply due to a coupling effect between the two lossless waveguides. Figure S8(b) shows the measured transmission spectra of this system with different bias magnetic fields. Figure S8(c) shows the results for three typical frequencies. As expected, we do not observe the enhanced transmission, indicating the important role of the microwave absorber. We also find with the increase of the bias magnetic field the cut-off shifts to higher frequencies. This is consistent with the theoretical prediction in the main text (see the dashed line in Fig. 4(c)).

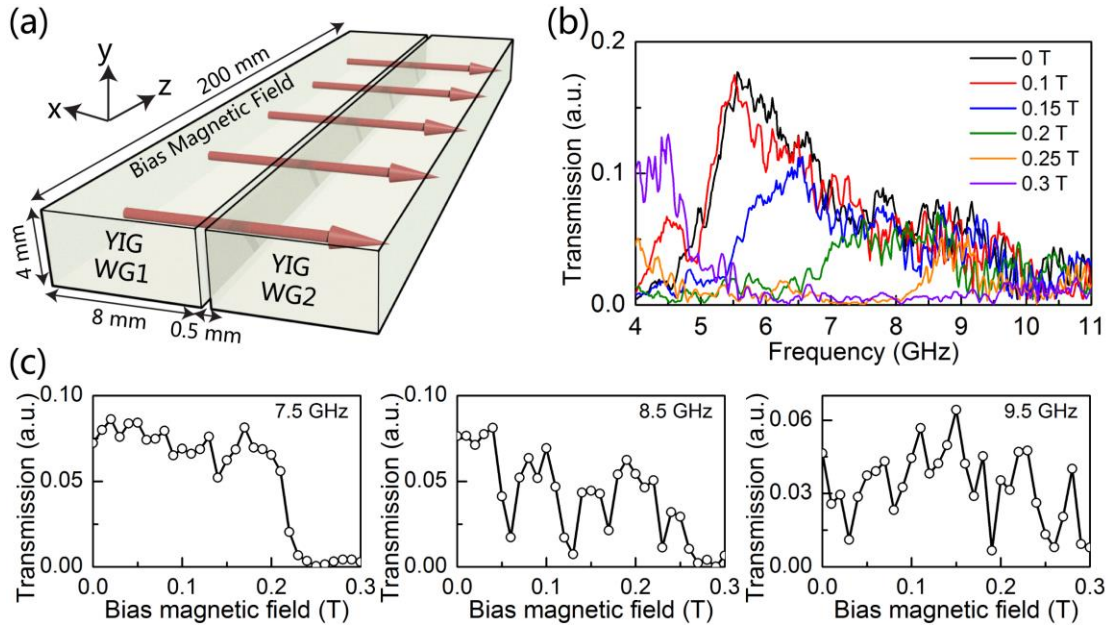


Figure S8. (a) Schematic of the coupled system without the microwave absorber. (b)-(c) Measured transmission spectra of this system.

7 Control experiment IV: single YIG waveguide with the microwave absorber

We perform a fourth control experiment by studying a single YIG waveguide with the microwave absorber, with the schematic illustrated in Fig. S9(a). The aim of this control experiment is to demonstrate that the observed transmission enhancement phenomenon is not simply due to the variation of mode losses when the bias magnetic field is changing. Figure S9(b) shows the measured transmission spectra of this system with different bias magnetic fields. It is found the transmission is almost unchanged because there is no other route, e.g., another lossless waveguide in the broken phase region, for the microwave to propagate through.

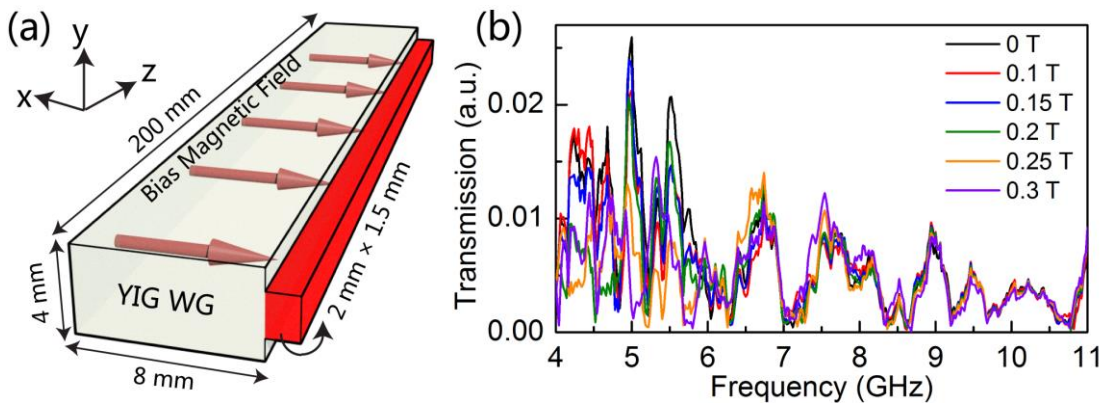


Figure S9. (a) Schematic of a single YIG waveguide with the microwave absorber. (b) Measured transmission spectra of this system.

8 Non-uniformity of the bias magnetic field

The external magnetic field acting on the coupled waveguide system with a length of 200 mm is actually not uniform, but we show in this part that this slight non-uniformity will not affect the phenomena expected in experiments. Figure S10(a) shows the measured bias magnetic fields at different positions (circles) and they are fitted with the solid line for numerical simulations. We then calculate the transmission spectrum at 9.5 GHz with this non-uniformity taken into account in Fig. S10(b), where the result with a uniform bias magnetic field is also given for reference. We see that there is only a slight shift of the transmission spectrum if the bias magnetic field is non-uniform but all the physics discussed in this work remain the same. This part can help understand the slight discrepancies between theory and experiment in Fig. 4(c).

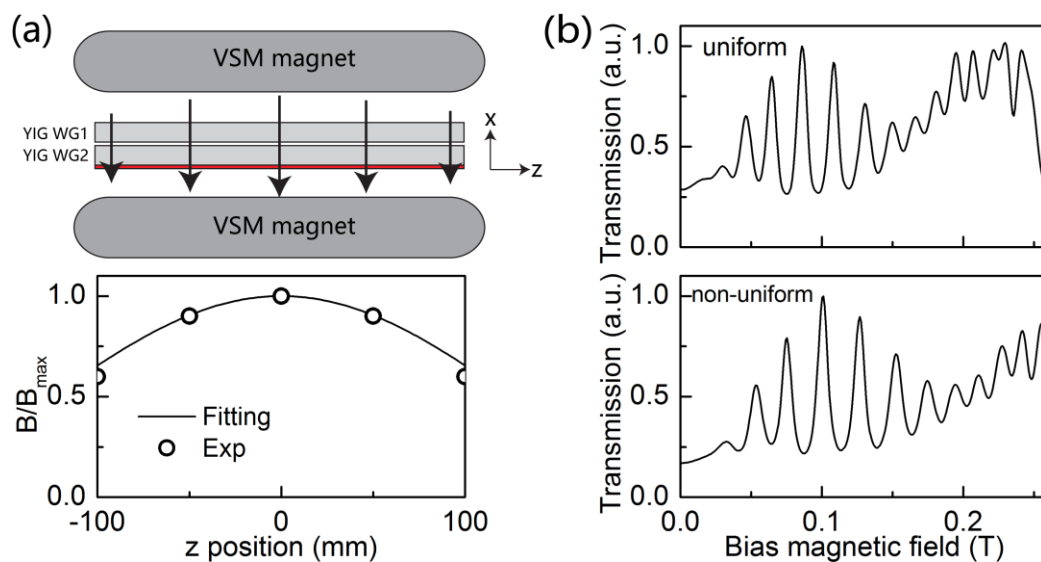


Figure S10. (a) Non-uniformity of the bias magnetic field acting on the system. (b) Calculated transmission spectra with uniform and non-uniform magnetic field.